Differentiating renal epithelioid angiomyolipoma from clear cell carcinoma: using a radiomics model combined with CT imaging characteristics

Taek Min Kim[1,2] · Hyungwoo Ahn[2,3] · Hyo Jeong Lee[1] · Min Gwan Kim[1] · Jeong Yeon Cho[1,2,4] · Sung Il Hwang[2,3] · Sang Youn Kim[1,2]

Abstract

Purpose This study aims to assess the computed tomography (CT) findings of renal epithelioid angiomyolipoma (EAML) and develop a radiomics-based model for differentiating EAMLs and clear cell renal cell carcinomas (RCCs).

Method This two-center retrospective study included 28 histologically confirmed EAMLs and 56 size-matched clear cell RCCs with preoperative three-phase kidney CTs. We conducted subjective image analysis to determine the CT parameters that can distinguish EAMLs from clear cell RCCs. Training and test sets were divided by chronological order of CT scans, and radiomics model was built using ten selected features among radiomics and CT features. The diagnostic performance of the radiomics model was compared with that of the three radiologists using the area under the receiver-operating characteristic curve (AUC).

Results The mean size of the EAMLs was 6.2 ± 5.0 cm. On multivariate analysis, a snowman or ice cream cone tumor shape (OR 16.3; 95% CI 1.7–156.9, $P = 0.02$) and lower tumor-to-cortex (TOC) enhancement ratio in the corticomedullary phase (OR 33.4; 95% CI 5.7–197, $P < 0.001$) were significant independent factors for identifying EAMLs. The diagnostic performance of the radiomics model (AUC 0.89) was similar to those of genitourinary radiologists (AUC 0.78 and 0.81, $P > 0.05$) and superior to that of a third-year resident (AUC 0.63, $P = 0.04$).

Conclusions A snowman or ice cream cone shape and lower TOC ratio were more closely associated with EAMLs than with clear cell RCCs. A CT radiomics model was useful for differentiating EAMLs from clear cell RCCs with better diagnostic performance than an inexperienced radiologist.

Keywords Angiomyolipoma · Epithelioid angiomyolipoma · Perivascular epithelioid cell neoplasm · Clear cell renal cell carcinoma · Computed tomography · Radiomics

Taek Min Kim, Hyungwoo Ahn have contributed equally as first authors.

✉ Sang Youn Kim
iwishluv@empas.com

[1] Department of Radiology, Seoul National University Hospital, Seoul, Korea

[2] Department of Radiology, Seoul National University College of Medicine, Seoul, Korea

[3] Department of Radiology, Seoul National University Bundang Hospital, Seongnam-si, Gyeonggi-do, Korea

[4] Institute of Radiation Medicine and Kidney Research Institute, Seoul National University Medical Research Center, Seoul 03080, Korea

Abbreviations

CT	Computed tomography
EAML	Epithelioid angiomyolipoma
GLRLM	Gray-level run length matrices
GLSZM	Gray-level size zone matrices
HU	Hounsfield units
ICC	Intra-class correlation coefficient
RCC	Renal cell carcinomas
ROC	Receiver-operating characteristic curve
ROI	Regions of interest
TOC	Tumor-to-cortex
WHO	World Health Organization

Introduction

Angiomyolipoma (AML) is the most common renal mesenchymal neoplasm [1]. Most AMLs contain macroscopic adipose tissues that can be easily identified via computed tomography (CT) or magnetic resonance imaging [2]. According to the 2016 World Health Organization (WHO) classification, renal epithelioid angiomyolipoma (EAML) is a rare variant of AML that consists predominantly of epithelioid cells (> 80%) [3]. Unlike typical AMLs, EAMLs contain minimal or no fat that can be recognized, possibly leading to a misdiagnosis of renal cell carcinomas (RCCs) in histologic and imaging evaluations [4]. When we encounter enhancing renal mass with no or minimal fat, differentiating EAML from RCC or fat-poor AML is challenging. However, because of the rarity of this disease, imaging findings of EAML have been less well reported [5–9]. Additionally, to the best of our knowledge, there are no reliable image findings for distinguishing EAMLs from RCCs in CT. Although EAML has been regarded as a potentially malignant mesenchymal neoplasm and treated with surgical resection, the optimal treatment and prognosis of EAML remain controversial and different from those of RCC [10]. Thus, the ability to distinguish EAML from RCC is clinically important.

Radiomics analysis offers quantitative image information that cannot be achieved by radiologists' visual interpretation [11]. It has been widely used to differentiate different types of renal tumors, including benign versus malignant tumors and RCC subtype classifications in cross-sectional images [12, 13]. Furthermore, recent studies reported accurate differentiation of fat-poor AML from RCC using radiomics-based model [14, 15]. In conjunction with subjective image features, a radiomics-based model may help to quantitatively distinguish EAMLs from RCCs.

In this study, we subjectively analyzed CT image findings of 28 EAMLs. Furthermore, we constructed a radiomics-based model combined with CT imaging characteristics to differentiate EAML from clear cell RCC and compared the diagnostic performance with that of radiologists. We selected clear cell RCC as the comparison tumor because clear cell RCC tend to be more hypervascular and heterogeneous appearance than other common subtypes including papillary and chromophobe RCC–the features that could overlap with EAML [16, 17].

# Materials and methods

Study cohort

This retrospective case–control study was approved by the institutional review board, and the requirement for written informed consent was waived. We searched the pathology database of two tertiary care institutions for surgical specimens diagnosed with renal EAMLs between January 2006 and June 2021: We identified 31 patients (16 in center A and 15 in center B). We excluded three patients who did not have three-phase kidney protocol CT, including precontrast, corticomedullary, and excretory phases. Finally, a total of 28 patients (15 men and 13 women, mean age 45.6 ± 13.7 years) were included (Fig. 1).

For the comparison group, we collected data on 56 patients with a diagnosis of clear cell RCC (38 men and 18 women, mean age 61.2 ± 11.7 years) during the same study period in center A. We matched the average maximal diameter of the masses between the EAML and clear cell RCC groups to eliminate the influence of the size on discrimination of the tumors. Patients who underwent CT scans before June 2017 were assigned to a training set (20 EAMLs and 40 clear cell RCCs), and the remaining patients were assigned to a test set (eight EAMLs and 16 clear cell RCCs).

Subjective image analysis

Two fellowship-trained radiologists with 7 years of experience in genitourinary imaging, who were blinded to the patients' information and histopathologic results, independently reviewed the CT scans of EAMLs and clear cell RCCs. Disagreement was resolved by a third radiologist with 17 years of experience in genitourinary imaging. We evaluated the following characteristics: maximal diameter of the mass; tumor laterality (right, left); tumor heterogeneity (homogeneous, heterogeneous); snowman or ice cream cone shape of the tumor; presence of calcification and fat; grade of tumor necrosis ($< 33\%$, $34–66\%$, $\geq 67\%$); tumor margin (well-defined, infiltrative); high attenuation on precontrast scan; enhancement pattern (wash-in and wash-out, persistent enhancement); tumor-to-cortex (TOC) enhancement ratio in the corticomedullary phase; presence of intratumoral or peritumoral vessels; renal vein invasion; lymph node metastasis; and distant metastasis.

Tumors were defined as homogeneous when > 90% of the area was occupied by the similar attenuation value via visual inspection; otherwise, they were considered heterogeneous. The snowman shape was defined as a bilobulated, dumbbell-like appearance. The ice cream cone shape was
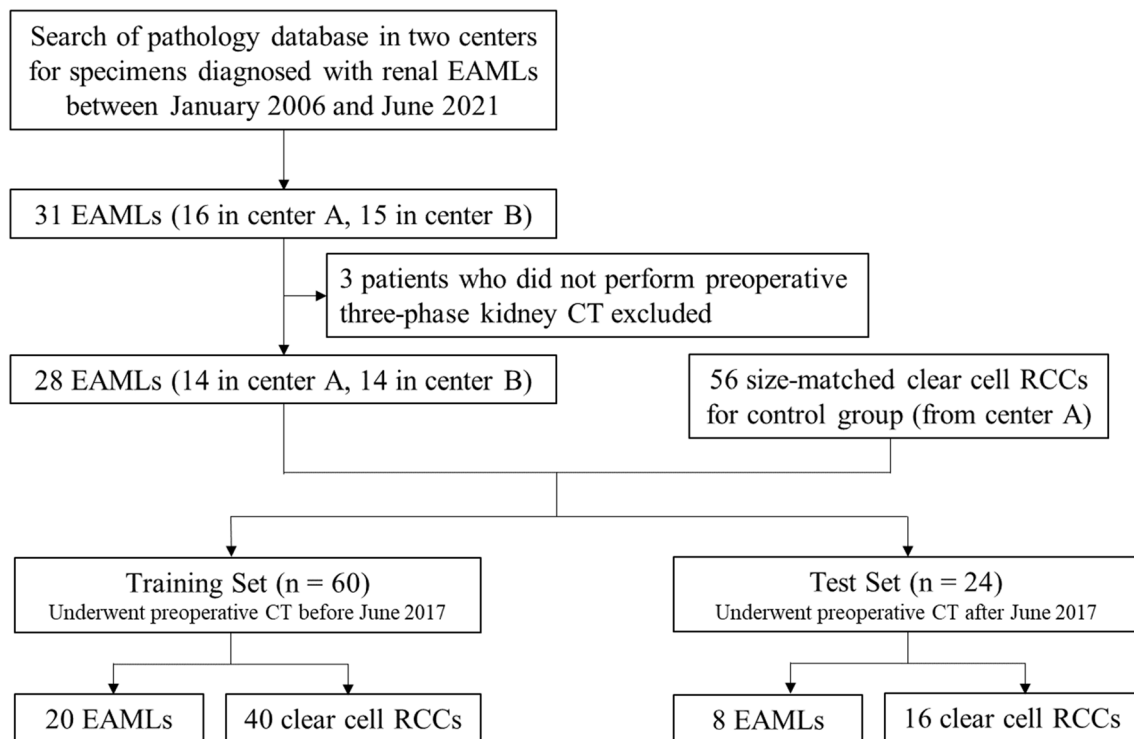
Fig. 1 Flowchart of patient selection in the study. *EAML* epithelioid angiomyolipoma, *RCC* renal cell carcinoma

considered present when the exophytic portion had a uniform rounded interface, whereas the endophytic portion had a tapering, pyramidal interface with a definable apex in the parenchyma, which was known to useful morphologic contour to predict AML [18]. In all three phases, we placed regions of interest (ROIs) as large as possible in the solid portion of the tumor, avoiding fat, necrotic, or hemorrhagic components. Additionally, we drew ROIs in the renal cortex in the precontrast and corticomedullary phases. The high attenuation on precontrast was defined as present when the attenuation of the mass was ≥ 10 Hounsfield units (HU) than that of the renal cortex. Wash-in and wash-out were considered present when the attenuation of the solid portion of the tumor decreased by ≥ 20 HU in the excretory phase as compared with the corticomedullary phase [19]; otherwise, the enhancement pattern was considered as a persistent enhancement. We calculated the TOC ratio by dividing the HU of the solid portion of the tumor by the HU of the renal cortex measured in the corticomedullary phase.

Tumor segmentation and feature extraction

We imported axial CT images of the precontrast and corticomedullary phases into commercially available software (MEDIP, medical IP). Lesions were semiautomatically segmented using intensity-based thresholding and the region-growing function in the corticomedullary phases. Subsequently, two radiologists manually and independently edited the margin of the tumors. The masks were copied and pasted to the precontrast image, and subsequent manual refinement was conducted.

We extracted the radiomics features by using syngo.via Frontier software (Siemens Healthineers), which was developed based on the PyRadiomics library (https://github.com/Radiomics/pyradiomics) and scikit-learn machine learning library (https://scikit-learn.org/stable/modules/generated/sklearn.ensemble.RandomForestClassifier.html). Images were resampled at a spatial resolution of $1 \times 1 \times 1$ mm^3 using linear interpolation and discretized with a bin width of 25 HU. Additionally, to minimize CT intensity changes and obtain more stable radiomics features, we normalized the intensity of the image using the following formula (where x represents the original intensity; f(x) represents the normalized intensity; μ indicates the average value; σ refers to variance; and s is an optional scaling ratio, which has been set to 1 by default) [20].

$$f(x) = \frac{s(x - \mu_x)}{\sigma_x}$$

A total of 110 radiomics features, including 18 first-order statistics, 17 shape features, 24 Gy-level co-occurrence matrices, 16 Gy-level run length matrices (GLRLMs),

16 Gy-level size zone matrices (GLSZMs), five neighboring gray tone difference matrices, and 14 Gy-level dependence matrices, were extracted. We extracted the radiomics features from both precontrast and corticomedullary phase images (220 features) and included 16 CT features obtained from the subjective image analysis. Excretory phase images were not used for radiomics analysis because of the different scan timing between two centers. Finally, we used a total of 236 features.

Feature selection and radiomics model development

Because radiomics features were vulnerable to segmented volumes of interest, we evaluated the agreement of the features between the volumes of interest. We excluded the radiomics features with an intra-class correlation coefficient (ICC) of < 0.75 in the interobserver study. The combined radiomics and subjective features were reduced to 10 features in the training set by classic minimum redundancy maximum relevance using the R^2 difference. This algorithm guarantees the selection of features that are highly relevant to actual classes while reducing redundancy among selected features [21]. By using the 10 selected features, a random forest model was constructed. We conducted tenfold cross-validation using the repetition of feature selection and model development for each subset. The average area under the receiver-operating characteristic curve (AUC) and average sensitivity, specificity, and accuracy with a threshold probability of 0.5 were provided as performance metrics for the training set. The final trained model was applied to the test set. Two fellowship-trained radiologists (readers 1 and 2) and a third-year resident (reader 3) in training independently reviewed the test set. They were blinded to the clinical information and were encouraged to decide whether each tumor was either an EAML or clear cell RCC.

Statistical analysis

In the group comparisons, we used Fisher's exact test for categorical variables and the Mann–Whitney U test for continuous variables, as appropriate. Subgroup analysis was conducted according to the size of the mass: < 4 cm, 4–7 cm, and ≥ 7 cm. To determine the independent risk factor for identifying EAMLs, we conducted multivariate logistic regression on the statistically significant parameters ($P < 0.05$) in the univariate analysis in the training set. Interobserver agreement was evaluated using the Cohen kappa coefficient for categorical variables and ICC for continuous variables. The kappa values were defined as follows: $\kappa < 0$, less than chance agreement; 0.01–0.20, slight agreement; 0.21–0.40, fair agreement; 0.41–0.60, moderate agreement; 0.61–0.80, substantial agreement; and 0.81–0.99, almost perfect agreement [22]. In

terms of ICC, values ≥ 0.75 were considered reproducible. To evaluate the performance of the prediction model on the training set and test set, we conducted a receiver-operating characteristic analysis. The AUC of the radiomics model was compared with that of the three readers. All statistical analyses were conducted using SPSS (version 25; IBM), and a $P < 0.05$ was considered statistically significant.

Results

Baseline characteristics of EAMLs

Table 1 summarizes the information on the baseline characteristics of patients with EAMLs. The mean size of the tumors was 6.2 ± 5.0 cm (range, 0.9–17.6 cm). Three patients (10.7%) had a history of tuberous sclerosis. One patient showed bone metastasis on diagnosis. Two patients were presented with lung metastases at 20 and 61 months after surgery, respectively. The remaining 25 patients had no evidence of tumor recurrence or distant metastasis during the median follow-up of 12.5 months (range, 1–137 months).

Comparison of CT findings between EAMLs and clear cell RCCs

The patients with EAML were significantly younger than those with clear cell RCC (45.6 ± 13.7 vs. 61.2 ± 11.7 years, $P < 0.001$). The mean mass size was 6.2 ± 5.5 cm in the EAML group and 5.5 ± 3.4 cm in the clear cell RCC group, and did not show significant difference (P = 0.43). In subjective image analysis, the EAMLs showed less heterogeneous appearance than the clear cell RCCs did (78.6% vs. 98.2%, $P = 0.002$) (Fig. 2). The EAMLs showed more frequent snowman or ice cream cone shape than the clear cell RCCs did (39.3% vs. 5.4%, $P = 0.002$) (Fig. 3). Four of the 28 EAMLs had a fat component, whereas only one in the clear cell RCC group did (14.3% vs. 1.8%, $P = 0.022$) (Fig. 4). The EAMLs tended to have smaller necrotic portions ($P < 0.001$) and well-defined margins (92.9% vs. 71.4%, $P = 0.024$) than clear cell RCCs did. Additionally, the EAMLs showed more frequent high attenuation on precontrast images (71.4% vs. 17.9%, $P < 0.001$), persistent enhancement (32.1% vs. 1.8%, $P < 0.001$), and lower TOC ratio in the corticomedullary phase (0.55 ± 0.18 vs. 0.91 ± 0.17, $P < 0.001$). We described the result of subgroup analysis according to mass size in Table 2 as well as supplementary content.

Univariate and multivariate analyses of CT parameters in identifying EAMLs

Table 3 presents detailed information regarding the univariate and multivariate analyses for identifying EAMLs in the training set. In the univariate analysis, homogeneous

Table 1 Baseline and radiological characteristics of the patients

Characteristics	Epithelioid AML (n=28)	Clear cell RCC (n=56)	P-value*
Age (years)	45.6±13.7	61.2±11.7	<0.001
Sex			0.20
Men	15 (57.7)	38 (67.9)	
Women	13 (42.3)	18 (32.1)	
Mass size (cm)	6.2±5.0	5.5±3.4	0.430
<4 cm	12 (42.8)	24 (42.8)	
4–7 cm	8 (28.6)	16 (28.6)	
≥7 cm	8 (28.6)	16 (28.6)	
Laterality			0.644
Right	16 (57.1)	29 (51.8)	
Left	12 (42.9)	27 (45.2)	
Tumor heterogeneity			0.002
Homogeneous	6 (21.4)	1 (1.8)	
Heterogeneous	22 (78.6)	55 (98.2)	
Snowman or ice cream cone shape	11 (39.3)	3 (5.4)	0.025
Calcification	2 (7.1)	9 (16.1)	0.253
Fat	4 (14.3)	1 (1.8)	0.022
Grade of necrosis			<0.001
<33%	15 (53.6)	11 (19.6)	
33–66%	7 (25)	41 (73.2)	
≥67%	6 (21.4)	4 (7.1)	
Margin			0.024
Well-defined	26 (92.9)	40 (71.4)	
Infiltrative	2 (7.1)	16 (28.6)	
High attenuation on precontrast	20 (71.4)	10 (17.9)	<0.001
Enhancement pattern			<0.001
Wash-in and wash-out	19 (67.9)	55 (98.2)	
Persistent enhancement	9 (32.1)	1 (1.8)	
Tumor-to-cortex enhancement ratio in CMP	0.55±0.18	0.91±0.17	<0.001
Intratumoral vessel	14 (50)	35 (62.5)	0.273
Peritumoral vessel	11 (39.2)	27 (48.2)	0.438
Renal vein invasion	1 (3.6)	10 (17.9)	0.067
Lymph node metastasis	0 (0)	1 (1.8)	0.477
Distant metastasis	1 (3.6)	3 (5.4)	0.717

AML angiomyolipoma, *RCC* renal cell carcinoma, *CMP* corticomedullary phase

Categorical variables are expressed as numbers of patients, with percentages in parentheses. Continuous variables are expressed as mean±standard deviation

*Continuous data were assessed using Mann–Whitney U test, while categorical data were assessed using Fisher's exact test

enhancement, snowman or ice cream cone tumor shape, lower grade of necrosis (<33%), well-defined margin, high attenuation on precontrast images, persistent enhancement, and lower TOC ratio in the corticomedullary phase (<0.7) were significant factors for identifying EAMLs ($P < 0.05$ for all). In the multivariate logistic regression, snowman or ice cream cone tumor shape (odds ratio [OR] 16.3; 95% confidence interval [CI] 1.7–156.9, $P = 0.02$) and lower TOC ratio in the corticomedullary phase (OR 33.4; 95%

CI 5.7–197, $P < 0.001$) were significant independent factors in terms of identifying EAMLs.

Radiomics feature extraction and development of the radiomics prediction model

Table 4 presents patient characteristics of the training and test sets. Among the 220 radiomics features extracted in the precontrast and corticomedullary phases, we excluded

Fig. 2 a–c A 49-year-old man with epithelioid angiomyolipoma. Unenhanced CT image showed a 2.1 cm tumor of high attenuation (48 HU) without gross fat in the right kidney upper pole (**a**). The tumor demonstrated mild enhancement in the corticomedullary phase (**b**) and homogeneous, persistent enhancement in the excretory phase (**c**). **d** A 75-year old man with clear cell renal cell carcinoma. The tumor showed almost similar enhancement with renal cortex in the corticomedullary phase, with heterogeneous appearance even in the small size

28 with inacceptable interobserver agreement on image segmentation (ICC < 0.75). Finally, we used 208 features (192 radiomics features and 16 subjective image features) to develop the radiomics prediction model. The 10 most relevant features selected from the training set were three subjective image features (snowman or ice cream cone tumor shape, high attenuation on precontrast images, and TOC ratio), five radiomics features from the corticomedullary phases (two first orders, one GLRLM, one GLSZM, and one shape feature), and two radiomics features from the precontrast phases (GLRLM and GLSZM). Figure 5 presents a heat map of the selected radiomics features between EAMLs and clear cell RCCs.

From the tenfold cross-validation, the average AUC of the radiomics model was 0.84, with a sensitivity of 90%, a specificity of 70%, and an accuracy of 77% in the training set. In the test set, the average AUC of the model was 0.89,

with a sensitivity of 62.5%, a specificity of 87.5%, and an accuracy of 79.2%.

Comparison between the radiomics model and radiologists

Table 5 and Fig. 6 present information on the diagnostic performance of the radiomics model and the three readers. The AUCs of the three readers were 0.81 (95% CI 0.60–0.94), 0.78 (0.57–0.92), and 0.63 (0.41–0.81) for readers 1, 2, and 3, respectively. The sensitivity and specificity of each reader were 87.5% and 75% for reader 1, 62.5% and 93.8% for reader 2, and 75.0% and 50.0% for reader 3, respectively. There were no significant differences between the AUCs of the radiomics prediction model and those of the reader 1 and 2 ($P = 0.55$
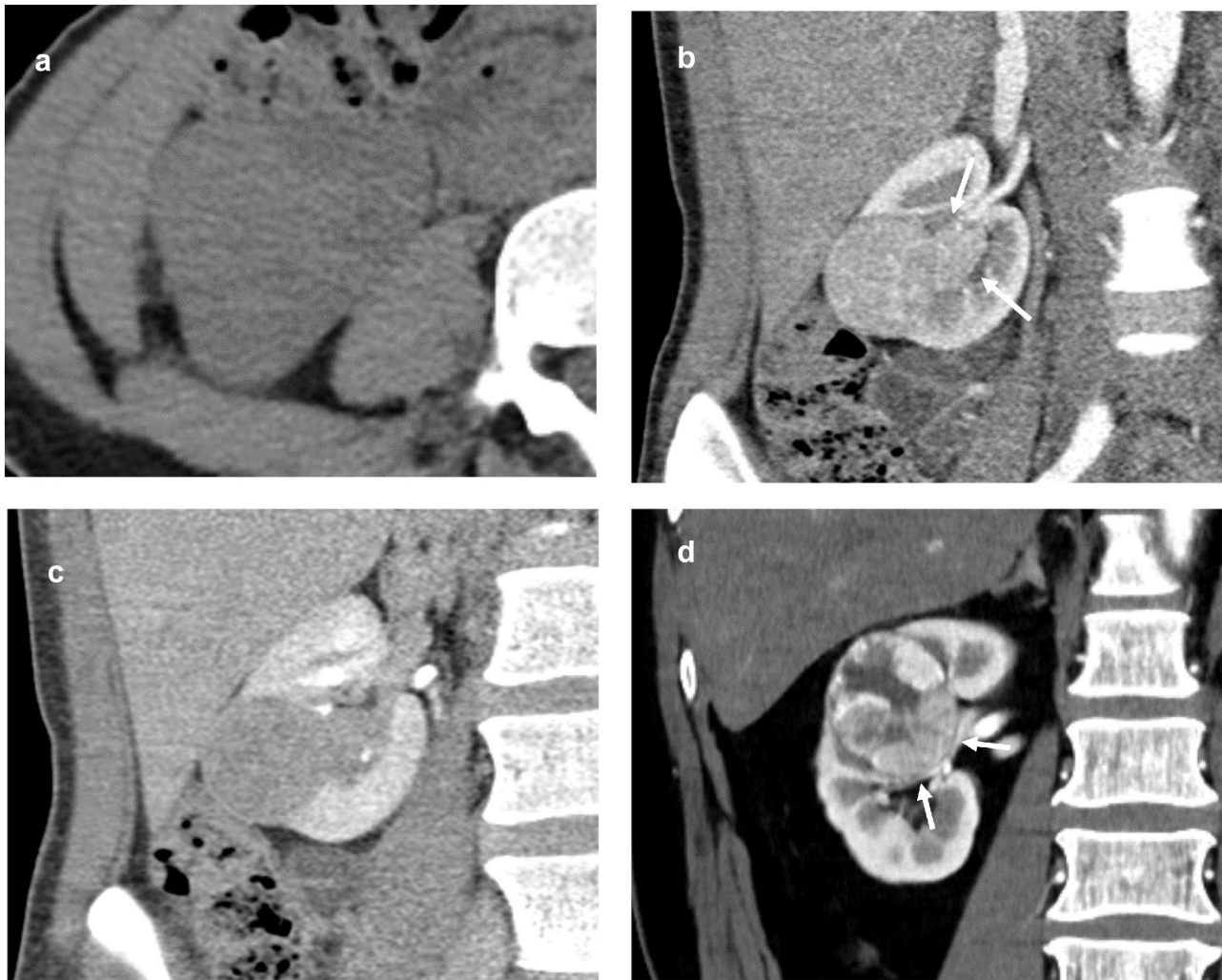
Fig. 3 a–c A 37-year-old woman with epithelioid angiomyolipoma. Unenhanced CT image showed a 4.6 cm tumor of mildly high attenuation (40 HU) without gross fat in the right kidney (**a**). The tumor was protruding to the renal sinus with bilobulated shape (arrows) and so-called snowman appearance in coronal image (**b**). In the excretory phase, the tumor showed delayed wash-out, with no delineable necrotic area (**c**). **d** A 61-year-old man with clear cell renal cell carcinoma. In contrast to the aforementioned case, the tumor protruded to renal sinus without any disturbance, destroying the normal renal architecture (arrows)

and 0.41, respectively). The AUC of the radiomics model was significantly higher than that of the reader 3 ($P = 0.04$).

Interobserver agreement

Table 6 summarizes the information of the interobserver agreements. Two readers showed moderate to almost perfect interobserver agreement for the categorical variables (κ: 0.60–1.0) and a reliable ICC (0.96) for TOC ratio measurement.

Discussion

Unlike other subtypes of AML, EAML is a potentially malignant tumor and can be locally aggressive or metastasize, thus surgical resection could be justified [17]. However, there might be significant differences in outcome for clear cell RCC and EAML. Clear cell RCCs have the lowest 5-year survival rate and the worst prognosis among
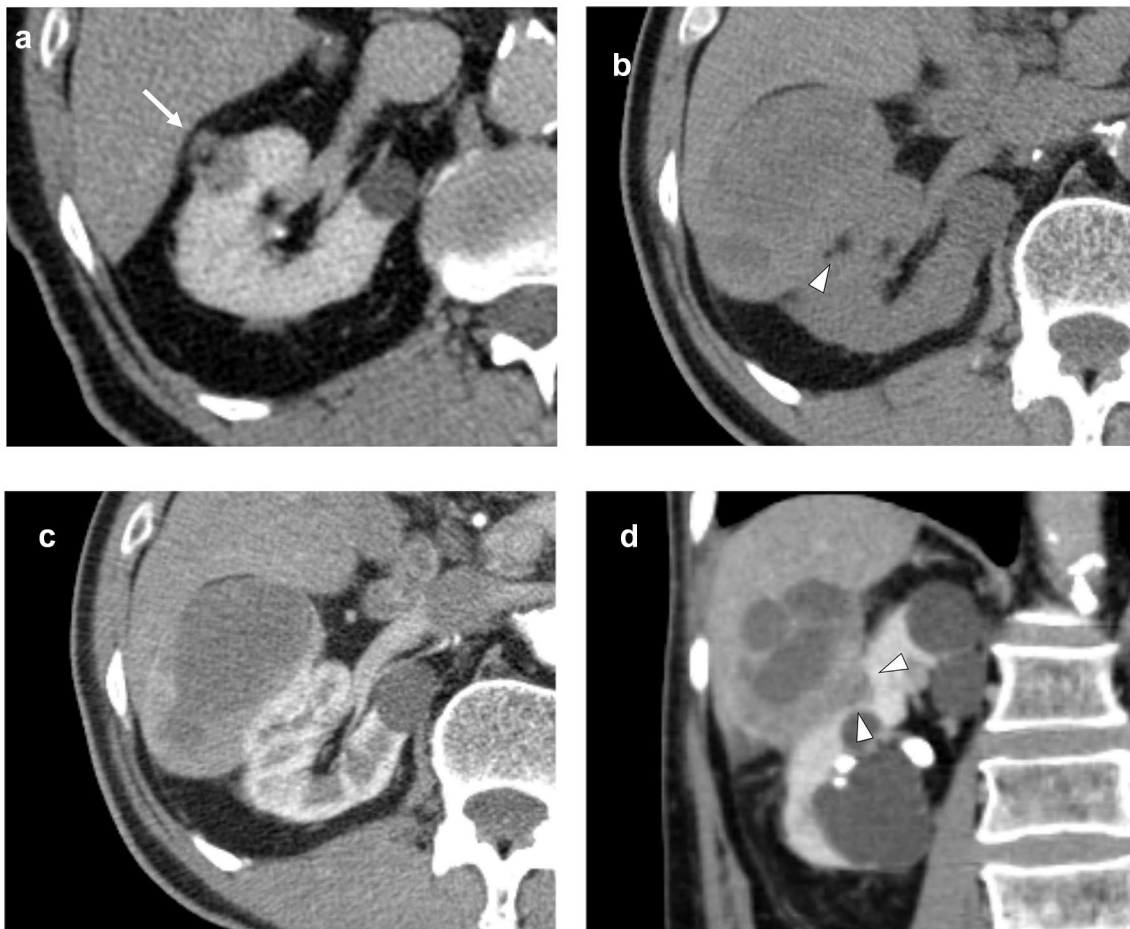
Fig. 4 A 77-year-old man with epithelioid angiomyolipoma. **a** A fat-containing solid mass was found in the right kidney (arrow). Initially, the lesion was interpreted as a classic angiomyolipoma. **b**–**d** After 3 years of follow-up, the size of the tumor increased to 7.2 cm. Unenhanced CT image (**b**) showed a focal fat component at the medial side of the tumor (arrowhead). The tumor showed heterogeneous contrast enhancement, areas of hemorrhage, and necrotic portion (**c**). In the coronal plane, the endophytic portion had a tapering interface (arrowheads), which showed an ice cream cone shape (**d**)

the RCC histologic subtypes, while EAML can exhibit various clinical course from benign to malignant behavior [23, 24]. Furthermore, clear cell RCC and EAML indicate different responses to the molecularly targeted therapies, especially in unresectable cases [25–28]. Hence, it is important to accurately differentiate EAML from clear cell RCC in imaging, which would be helpful for planning treatment strategies and precision medicine. We analyzed the CT findings of EAMLs and developed a radiomics-based model to differentiate EAMLs from clear cell RCCs. A radiomics-based model was developed from the radiomics features and the subjective image findings, which could be achieved from the CT images. By using this non-invasive information, the radiomics-based model showed good performance in distinguishing EAMLs and clear cell RCCs (AUC 0.89), which was similar to that of genitourinary radiologists (AUC 0.81 and 0.78) and superior to that of a third-year resident (AUC 0.62). To

our knowledge, this is the first study to compare the CT findings between the EAML and clear cell RCC, which are difficult to differentiate.

EAML is predominantly composed of epithelioid cells, and according to the 2016 WHO classification, the tumor contains almost no fat. The results from several previous reports also suggest that the EAML has no or a very small volume of fat component in imaging [6, 8, 9]. Similar to these results, fat was detected in only four of the 28 cases in our study. The remaining 24 lesions, which had no definite fat in the precontrast image, were mostly misdiagnosed as RCCs or renal sarcomas in our radiologic reports. These results demonstrate the importance of knowing the different CT manifestations between EAML and RCC.

We found some useful CT findings for distinguishing EAML from clear cell RCC. The snowman or ice cream cone shape of the tumor was one of the independent factors for identifying EAML. The ice cream cone shape or

Table 2 Comparison of radiologic characteristics between EAML and clear cell RCC according to the size

Characteristics	< 4 cm			4–7 cm			≥ 7 cm		
	Epithe-lioid AML (n = 12)	Clear cell RCC (n = 24)	P-value*	Epithe-lioid AML (n = 8)	Clear cell RCC (n = 16)	P-value*	Epithe-lioid AML (n = 8)	Clear cell RCC (n = 16)	P-value*
Tumor heterogeneity			0.001			–			–
Homogeneous	6 (50)	1 (4.2)		0 (0)	0 (0)		0 (0)	0 (0)	
Heterogeneous	6 (50)	23 (95.8)		8 (100)	16 (100)		8 (100)	16 (100)	
Snowman or ice cream cone shape	4 (33.3)	2 (8.3)	0.058	7 (87.5)	1 (6.3)	< 0.001	0 (0)	0 (0)	–
Calcification	1 (8.3)	0 (0)	0.15	0 (0)	6 (37.5)	0.046	1 (12.5)	3 (18.8)	0.70
Fat	0 (0)	0 (0)	–	1 (12.5)	0 (0)	0.15	3 (37.5)	1 (6.3)	0.053
Grade of necrosis			0.058			0.001			0.046
< 33%	10 (83.3)	10 (41.6)		5 (62.5)	1 (6.3)		0 (0)	0 (0)	
33–66%	2 (16.7)	13 (54.2)		1 (12.5)	14 (87.5)		4 (50)	14 (87.5)	
≥ 67%	0 (0)	1 (4.2)		2 (25)	1 (6.3)		4 (50)	2 (12.5)	
Margin			1.0			0.12			0.02
Well-defined	11 (91.7)	22 (91.7)		8 (100)	12 (75)		7 (87.5)	6 (37.5)	
Infiltrative	1 (8.3)	2 (8.3)		0 (0)	4 (25)		1 (12.5)	10 (62.5)	
High attenuation on pre-contrast	9 (75)	5 (20.8)	0.002	6 (75)	1 (6.3)	< 0.001	5 (62.5)	4 (25)	0.07
Enhancement pattern			0.04			0.009			0.013
Wash-in and wash-out	10 (83.3)	24 (100)		5 (62.5)	16 (100)		4 (50)	15 (93.8)	
Persistent enhancement	2 (16.7)	0 (0)		3 (37.5)	0 (0)		4 (50)	1 (6.2)	
Tumor-to-cortex enhancement ratio in CMP	0.61 ± 0.15	0.93 ± 0.18	< 0.001	0.53 ± 0.16	0.88 ± 0.16	< 0.001	0.48 ± 0.22	0.92 ± 0.18	< 0.001
Intratumoral vessel	1 (8.3)	3 (12.5)	0.71	7 (87.5)	16 (100)	0.15	6 (75)	16 (100)	0.037
Peritumoral vessel	1 (8.3)	4 (16.7)	0.50	3 (37.5)	8 (50)	0.56	7 (87.5)	15 (93.8)	0.06
Renal vein invasion	0 (0)	0 (0)	–	1 (12.5)	3 (18.8)	0.70	0 (0)	7 (43.8)	0.026
Lymph node metastasis	0 (0)	0 (0)	–	0 (0)	0 (0)	–	0 (0)	1 (6.3)	0.47
Distant metastasis	0 (0)	0 (0)	–	0 (0)	0 (0)	–	1 (12.5)	3 (18.8)	0.70

AML angiomyolipoma, *RCC* renal cell carcinoma, *CMP* corticomedullary phase

Categorical variables are expressed as numbers of patients, with percentages in parentheses. Continuous variables are expressed as mean ± standard deviation

*Continuous data were assessed using Mann–Whitney U test, while categorical data were assessed using Fisher's exact test

so-called angular interface has been known to be accurate for characterizing benign renal tumors, especially in the exophytic location [18, 29]. The snowman shape also suggests that the tumor was compressed by the adjacent renal parenchyma in the waist of the mass, which is a more favorable finding of a benign tumor. In our study, five EAMLs with exophytic location exhibited an ice cream cone shape, and five with endophytic location showed a snowman shape. Additionally, this finding was especially common in 4–7 cm EAMLs (87.5%). The EAMLs had more frequent snowman or ice cream cone shape than the clear cell RCCs only in the lesions with 4–7 cm, but not in < 4 cm or ≥ 7 cm. Thus, this distinctive shape could be used intuitively and usefully to distinguish EAML and clear cell RCC in moderately sized renal masses. Additionally, our result is inconsistent with the previous study by Kim et al., that ice cream cone shape

showed significant difference between RCC and fat-poor AML in small size (< 3 cm) [18]. Although fat-poor AML does not contain enough fat to be detected with images, it can have up to 25% fat cells per high-power field [30]. However, EAMLs predominantly consist of epithelioid component with few or no fat cells. These different histologic compositions between EAML and fat-poor AML could result the discrepancy in tumor shape.

Several imaging findings consistently showed a difference between EAML and clear cell RCC regardless of tumor size. The hyperattenuation on unenhanced CT of EAML has been reported in previous studies, and this might be due to the significant amount of epithelial muscle component [8, 10]. Our study was also consistent with previous results, and the findings on imaging were useful for distinguishing EAMLs from clear cell RCCs (71.4% vs. 17.9%). Both enhancement

Table 3 Univariate and multivariate analyses of CT parameters in identifying epithelioid angiomyolipoma

Parameters	Univariate analysis		Multivariate analysis*	
	Odds ratio (95% CI)	*P*-value	Odds ratio (95% CI)	*P*-value
Tumor heterogeneity (Homogeneous)	15.0 (1.7–131.9)	<0.01	21.0 (0.7–633)	0.08
Snowman or ice cream cone shape	11.4 (2.9–45.8)	<0.01	16.3 (1.7–156.9)	0.02
Calcification	0.4 (0.08–2.0)	0.27		
Fat	9.2 (1.0–86.4)	0.05		
Grade of necrosis (<33%)	4.7 (1.7–12.7)	<0.01	1.2 (0.2–8.4)	0.81
Margin (Well-defined)	5.2 (1.1–24.5)	0.04	7.6 (0.5–115.3)	0.14
High attenuation on precontrast	11.5 (3.9–33.4)	<0.01	2.9 (0.5–18.7)	0.26
Enhancement pattern (Persistent enhancement)	26.1 (3.1–219.4)	<0.01	8.4 (0.2–314)	0.25
Tumor-to-cortex enhancement ratio in CMP (<0.7)	30.6 (8.9–105.3)	<0.01	33.4 (5.7–197)	<0.01
Intratumoral vessel	0.6 (0.2–1.5)	0.28		
Peritumoral vessel	0.7 (0.3–1.7)	0.44		
Renal vein invasion	0.2 (0.02–1.4)	0.1		
Lymph node metastasis	–	1.0		
Distant metastasis	0.7 (0.06–6.6)	0.72		

CI confidence interval, *CMP* corticomedullary phase

*Multivariate logistic regression was performed on the parameters that were statistically significant ($P<0.05$) in the univariate analysis in the training set

pattern and degree have been known to reflect the microvessel densities of the tumors, and they were also different between EAML and clear cell RCC [31]. The clear cell RCC group typically showed almost the same enhancement as the cortex in the corticomedullary phase (TOC ratio 0.91) and a frequent wash-out in the excretory phase (98.2%), the so-called "fast in and fast out" [30]. By contrast, the EAML group showed a lower enhancement ratio (TOC ratio 0.55) and less frequent wash-out (67.9%) than the RCC group did, which was similar to the results reported by Luo et al. (TOC ratio 0.64, slow wash-out 68%) [32].

Table 4 Patient characteristics in the training and test sets

| Characteristics	Training set (n=60)	Test set (n=24)	*P*-value*
Age (years)	56.6±14.9	54.5±12.8	0.41
Sex			0.66
Men	37 (61.7)	16 (66.7)	
Women	23 (38.3)	8 (33.3)	
Pathology			1.0
Epithelioid AML	20 (33.3)	8 (33.3)	
Clear cell RCC	40 (66.7)	16 (66.7)	
Mass size (cm)	5.5±3.7	6.3±4.8	0.45

AML angiomyolipoma, *RCC* renal cell carcinoma

Categorical variables are expressed as numbers of patients, with percentages in parentheses. Continuous variables are expressed as mean±standard deviation

*Continuous data were assessed using Mann–Whitney U test, while categorical data were assessed using Fisher's exact test

Tumor necrosis is known to be common in EAML as a result of active tumor cell proliferation and insufficient internal blood supply [9, 32]. Nevertheless, the clear cell RCC group tended to demonstrate a higher grade of necrosis than the EAML group did. Additionally, EAMLs <4 cm in size tended to be homogeneous (50%), whereas most of the clear cell RCCs <4 cm were heterogeneous (95.8%), even in the small size. These findings might have contributed to the difference in the growth pattern of tumor cells and the degree of nuclear atypia between definite malignant tumors and tumors with malignant potential [33].

Among the clear cell RCCs ≥7 cm in this study, 81.2% (13/16) were surgically proven to have perirenal fat invasion and 43.8% (7/16) had renal vein involvement. These pathologic results might be associated with the CT findings of infiltrative margin and gross renal vein invasion of the tumors. Because an RCC >7 cm has higher risk of perirenal fat invasion or renal vein involvement, a large renal mass with a well-defined margin and absence of renal vein thrombosis would more likely suggest EAML than clear cell RCC [34].

Interestingly, the results of the radiomics features finally selected for the radiomics-based model confirm the results of the visual interpretation. The first-order features from the corticomedullary phase (90th percentile and root mean squared) that were decreased in the EAML group would be attributed to a relatively lesser degree of enhancement of the EAMLs than that of clear cell RCCs. The TOC ratio, which was obtained by a radiologist, was also included among the final 10 features, confirming previous findings.
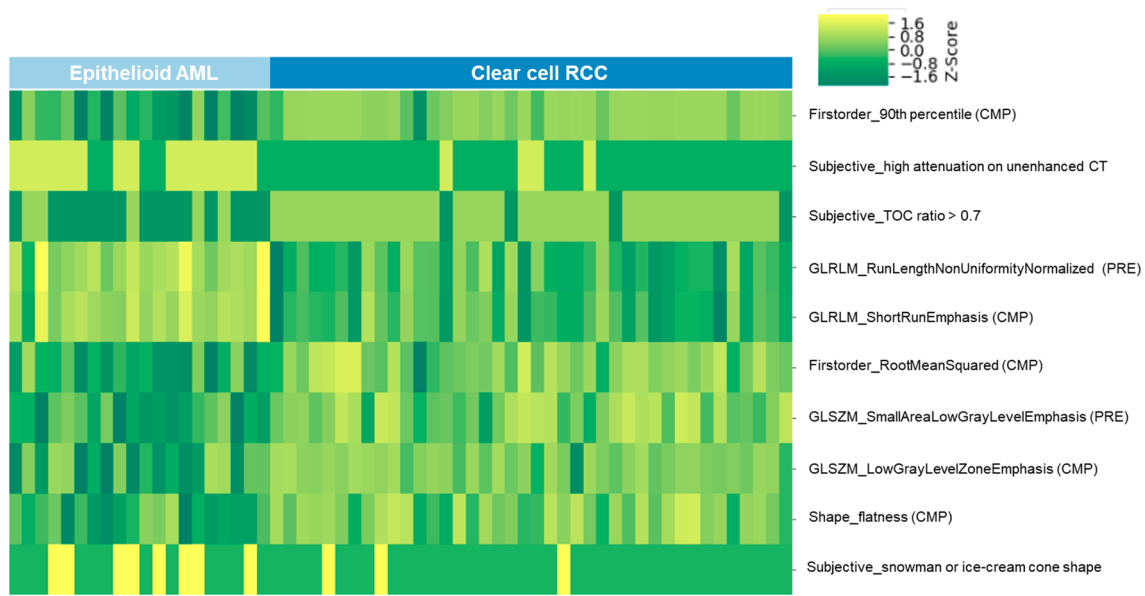
Fig. 5 Heat map of the 10 most relevant radiomics features for differentiating between EAMLs and clear cell RCCs. *AML* angiomyolipoma, *RCC* renal cell carcinoma, *CMP* corticomedullary phase, *TOC* tumor-to-cortex, *GLRLM* gray-level run length matrix, *PRE* precontrast phase, *GLSZM* gray-level size zone matrix

Table 5 Diagnostic performance of the radiomics prediction model and the three readers in the test set

Parameter	Radiomics model	Reader 1	Reader 2	Reader 3
AUC*	0.89 (0.69–0.98)	0.81 (0.60–0.94)	0.78 (0.57–0.92)	0.63 (0.41–0.81)
Sensitivity (%)	62.5 (5/8)	87.5 (7/8)	62.5 (5/8)	75.0 (6/8)
Specificity (%)	87.5 (14/16)	75 (12/16)	93.8 (15/16)	50.0 (8/16)
Accuracy (%)	79.2 (19/24)	79.2 (19/24)	83.3 (20/24)	58.3 (14/24)

AUC area under the curve

*Data in parentheses are 95% confidence intervals. There were no significant differences between the AUCs of the radiomics prediction model and those of reader 1 and 2 ($P = 0.55$ and 0.41, respectively). However, the AUC of the radiomics model was significantly higher than that of reader 3 ($P = 0.04$)

The three-dimension shape features from both radiomics (flatness, ranging from 1 [non-flat, sphere-like] to 0 [flat, non-sphere-like]) and from visual interpretation (snowman or ice cream cone shape) were included among the final 10 features. In concordance with the subjective assessment, flatness was significantly lower in the EAML group, suggesting the non-sphere-like shape of the EAMLs. Furthermore, the GLRLM and GLSZM features that were included in the radiomics model might reflect the difference of heterogeneity and necrotic portion between the EAML and clear cell RCC.

The present study had several limitations. First, the retrospective design might have introduced a selection bias. Additionally, although the study was conducted in two centers, the sample size was small. However, this was avoidable because of the rare nature of EAML. Second, CT images were acquired from different CT scanners with heterogeneous CT parameters, which could have influenced the results of the obtained radiomics parameters [35]. However, we tried to minimize this limitation using several processes, including voxel size resampling, CT number normalization, and exclusion of excretory phase images acquired at different times in two centers [20, 36]. Consequently, we obtained a radiomics-based model with acceptable accuracy in the test set. Third, we did not evaluate the percentage of the epithelioid component. The percentage of epithelioid component affects the CT manifestation between EAML and AML, with a recent study reporting a radiologic–pathologic correlation in the epithelioid component [32]. Finally, EAMLs can be also misdiagnosed as other renal tumors, such as fat-poor AML or non-clear cell RCC, but we did not include this analysis. Further comparison with renal tumors other than clear cell RCC is warranted.

In conclusion, our study found that EAML has characteristic CT signs that can be distinguished from clear cell RCC. Furthermore, our radiomics-based model has the potential to differentiate EAML and clear cell RCC with better

Fig. 6 Receiver-operating characteristic curve (ROC) of the radiomics model and those of the three readers for differentiating epithelioid angiomyolipoma and clear cell renal cell carcinoma in the test set. The area under the ROC curve of the radiomics model was comparable with those of two genitourinary radiologists (reader 1 and 2, $P=0.55$ and 0.41, respectively), and higher than that of a third-year resident (reader 3, $P=0.04$)
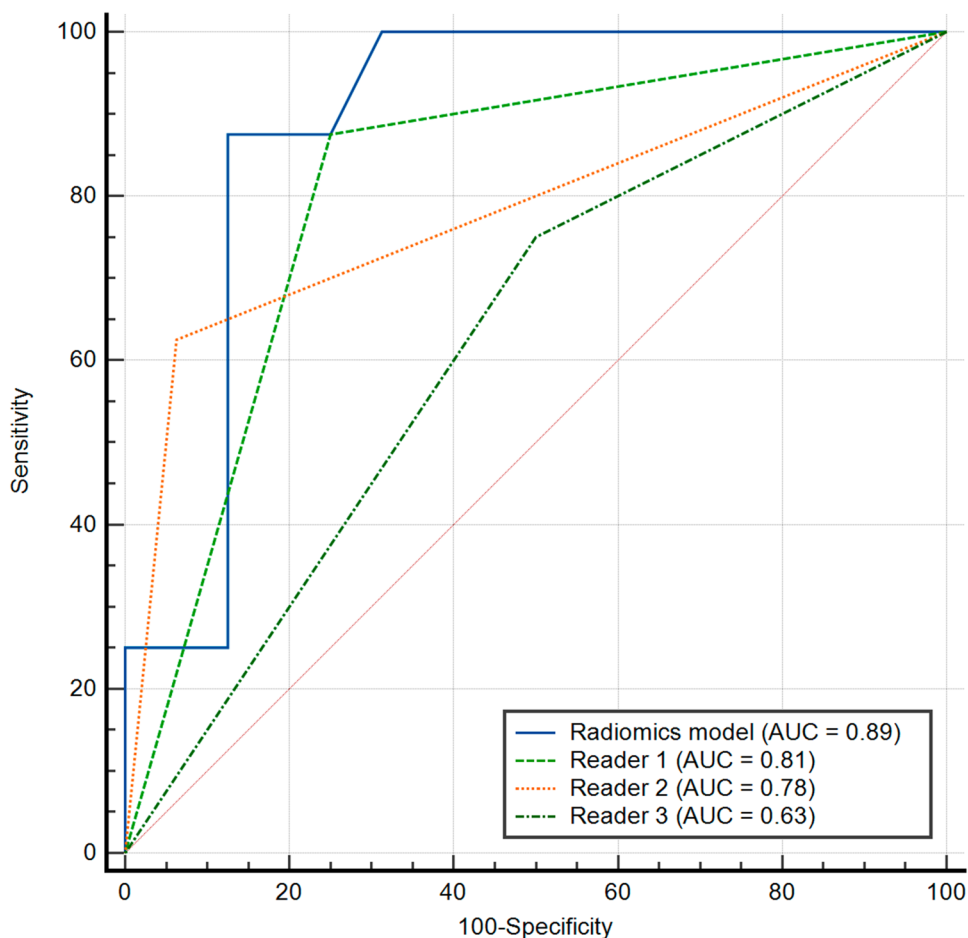
Table 6 Interobserver agreements of CT parameters in subjective image analysis in the study population between two readers

	Agreement*	Standard error	95% CI
Tumor heterogeneity	0.60	0.18	0.26–0.95
Snowman or ice cream cone shape	0.67	0.13	0.41–0.93
Calcification	1.0	0	1.0–1.0
Fat	1.0	0	1.0–1.0
Grade of necrosis	0.69	0.11	0.48–0.90
Margin	0.79	0.12	0.56–1.0
High attenuation on precontrast	0.73	0.11	0.51–0.95
Enhancement pattern	0.68	0.15	0.40–0.97
Tumor-to-cortex enhancement ratio in CMP	0.96	–	0.94–0.98
Intratumoral vessel	0.89	0.08	0.73–1.0
Peritumoral vessel	0.83	0.09	0.66–1.0
Renal vein invasion	1.0	0	1.0–1.0
Lymph node metastasis	1.0	0	1.0–1.0
Distant metastasis	1.0	0	1.0–1.0

CI confidence interval, *CMP* corticomedullary phase

*Agreements regarding categorical and continuous variables were assessed with Cohen's κ statistics and intra-class correlation coefficients (ICC), respectively

diagnostic performance compared with that of an inexperienced radiologist and could be useful when choosing treatment strategies in patients with indeterminate renal masses.

Declarations

Conflict of interest The authors have no competing interests to declare that are relevant to the content of this article.

Ethical approval This retrospective study was approved by the institutional review board in our center, and the requirement for written informed consent was waived.

References

1. Park BK (2017) Renal Angiomyolipoma: Radiologic Classification and Imaging Features According to the Amount of Fat. Am J Roentgenol 209:826–835. https://doi.org/10.2214/AJR.17.17973
2. Thiravit S, Teerasamit W, Thiravit P (2018) The different faces of renal angiomyolipomas on radiologic imaging: a pictorial review. Br J Radiol 20170533. https://doi.org/10.1259/bjr.20170533
3. Moch H, Cubilla AL, Humphrey PA, et al (2016) The 2016 WHO Classification of Tumours of the Urinary System and Male Genital Organs—Part A: Renal, Penile, and Testicular Tumours. Eur Urol 70:93–105. https://doi.org/10.1016/j.eururo.2016.02.029
4. Faraji H, Nguyen BN, Mai KT (2009) Renal epithelioid angiomyolipoma: a study of six cases and a meta-analytic study. Development of criteria for screening the entity with prognostic significance. Histopathology 55:525–534. https://doi.org/10.1111/j.1365-2559.2009.03420.x
5. Bharwani N, Christmas TJ, Jameson C, et al (2009) Epithelioid angiomyolipoma: imaging appearances. Br J Radiol 82:e249–e252. https://doi.org/10.1259/bjr/27259024
6. Cong X, Zhang J, Xu X, et al (2018) Renal epithelioid angiomyolipoma: magnetic resonance imaging characteristics. Abdom Radiol 43:2756–2763. https://doi.org/10.1007/s00261-018-1548-6
7. Cui L, Zhang J-G, Hu X-Y, et al (2012) CT imaging and histopathological features of renal epithelioid angiomyolipomas. Clin Radiol 67:e77–e82. https://doi.org/10.1016/j.crad.2012.08.006
8. Froemming AT, Boland J, Cheville J, et al (2013) Renal Epithelioid Angiomyolipoma: Imaging Characteristics in Nine Cases With Radiologic-Pathologic Correlation and Review of the Literature. Am J Roentgenol 200:W178–W186. https://doi.org/10.2214/AJR.12.8776
9. Tsukada J, Jinzaki M, Yao M, et al (2013) Epithelioid angiomyolipoma of the kidney: Radiological imaging: Imaging of epithelioid angiomyolipoma. Int J Urol 20:1105–1111. https://doi.org/10.1111/iju.12117
10. Lei JH, Liu LR, Wei Q, et al (2015) A Four-Year Follow-up Study of Renal Epithelioid Angiomyolipoma: A Multi-Center Experience and Literature Review. Sci Rep 5:10030. https://doi.org/10.1038/srep10030
11. Gillies RJ, Kinahan PE, Hricak H (2016) Radiomics: Images Are More than Pictures, They Are Data. Radiology 278:563–577. https://doi.org/10.1148/radiol.2015151169
12. Suarez-Ibarrola R, Basulto-Martinez M, Heinze A, et al (2020) Radiomics Applications in Renal Tumor Assessment: A Comprehensive Review of the Literature. Cancers 12:1387. https://doi.org/10.3390/cancers12061387
13. Sun X-Y, Feng Q-X, Xu X, et al (2020) Radiologic-Radiomic Machine Learning Models for Differentiation of Benign and Malignant Solid Renal Masses: Comparison With Expert-Level Radiologists. AJR Am J Roentgenol 214:W44–W54. https://doi.org/10.2214/AJR.19.21617
14. Feng Z, Rong P, Cao P, et al (2018) Machine learning-based quantitative texture analysis of CT images of small renal masses: Differentiation of angiomyolipoma without visible fat from renal cell carcinoma. Eur Radiol 28:1625–1633. https://doi.org/10.1007/s00330-017-5118-z
15. Ma Y, Ma W, Xu X, et al (2021) A convention-radiomics CT nomogram for differentiating fat-poor angiomyolipoma from clear cell renal cell carcinoma. Sci Rep 11:4644. https://doi.org/10.1038/s41598-021-84244-3
16. Young JR, Margolis D, Sauk S, et al (2013) Clear Cell Renal Cell Carcinoma: Discrimination from Other Renal Cell Carcinoma Subtypes and Oncocytoma at Multiphasic Multidetector CT. Radiology 267:444–453. https://doi.org/10.1148/radiol.13112617
17. Tsai C-C, Wu W-J, Li C-C, et al (2009) Epithelioid Angiomyolipoma of the Kidney Mimicking Renal Cell Carcinoma: A Clinicopathologic Analysis of Cases and Literature Review. Kaohsiung J Med Sci 25:133–140. https://doi.org/10.1016/S1607-551X(09)70052-X
18. Kim KH, Yun BH, Jung SI, et al (2013) Usefulness of the Ice-Cream Cone Pattern in Computed Tomography for Prediction of Angiomyolipoma in Patients With a Small Renal Mass. Korean J Urol 54:504–509. https://doi.org/10.4111/kju.2013.54.8.504
19. Israel GM, Bosniak MA (2008) Pitfalls in Renal Mass Evaluation and How to Avoid Them. RadioGraphics 28:1325–1338. https://doi.org/10.1148/rg.285075744
20. Chen X, Huang Y, He L, et al (2020) CT-Based Radiomics to Differentiate Pelvic Rhabdomyosarcoma From Yolk Sac Tumors in Children. Front Oncol 10:
21. Yu L, Liu H (2004) Efficient Feature Selection via Analysis of Relevance and Redundancy. J Mach Learn Res 5:1205–1224
22. Viera AJ, Garrett JM Understanding Interobserver Agreement: The Kappa Statistic. Fam Med 4
23. Cheville JC, Lohse CM, Zincke H, et al (2003) Comparisons of Outcome and Prognostic Features Among Histologic Subtypes of Renal Cell Carcinoma. Am J Surg Pathol 27:612–624
24. Brimo F, Robinson B, Guo C, et al (2010) Renal Epithelioid Angiomyolipoma With Atypia: A Series of 40 Cases With Emphasis on Clinicopathologic Prognostic Indicators of Malignancy. Am J Surg Pathol 34:715–722. https://doi.org/10.1097/PAS.0b013e3181d90370
25. Espinosa M, Roldán-Romero JM, Duran I, et al (2018) Advanced sporadic renal epithelioid angiomyolipoma: case report of an extraordinary response to sirolimus linked to TSC2 mutation. BMC Cancer 18:561. https://doi.org/10.1186/s12885-018-4467-6

26. Kohno J, Matsui Y, Yamasaki T, et al (2013) Role of mammalian target of rapamycin inhibitor in the treatment of metastatic epithelioid angiomyolipoma: A case report. Int J Urol 20:938–941. https://doi.org/10.1111/iju.12095

27. Saoud R, Kristof TW, Judge C, et al (2022) Clinical and pathological features of renal epithelioid angiomyolipoma (PEComa): A single institution series. Urol Oncol Semin Orig Investig 40:18–24. https://doi.org/10.1016/j.urolonc.2021.09.010

28. Escudier B, Porta C, Schmidinger M, et al (2019) Renal cell carcinoma: ESMO Clinical Practice Guidelines for diagnosis, treatment and follow-up. Ann Oncol 30:706–720. https://doi.org/10.1093/annonc/mdz056

29. Verma SK, Mitchell DG, Yang R, et al (2010) Exophytic Renal Masses: Angular Interface with Renal Parenchyma for Distinguishing Benign from Malignant Lesions at MR Imaging. Radiology 255:501–507. https://doi.org/10.1148/radiol.09091109

30. Jinzaki M, Silverman SG, Akita H, et al (2017) Diagnosis of Renal Angiomyolipomas: Classic, Fat-Poor, and Epithelioid Types. Semin Ultrasound CT MRI 38:37–46. https://doi.org/10.1053/j.sult.2016.11.001

31. Jinzaki M, Tanimoto A, Mukai M, et al (2000) Double-Phase Helical CT of Small Renal Parenchymal Neoplasms: Correlation with Pathologic Findings and Tumor Angiogenesis. J Comput Assist Tomogr 24:835–842

32. Luo C, Liu Z, Gao M, et al (2021) Renal epithelioid angiomyolipoma: computed tomography manifestation and radiologic–pathologic correlation depending on different epithelioid component percentages. Abdom Radiol. https://doi.org/10.1007/s00261-021-03313-3

33. He W, Cheville JC, Sadow PM, et al (2013) Epithelioid angiomyolipoma of the kidney pathological features and clinical outcome in a series of consecutively resected tumors. Mod Pathol Off JUS Can Acad Pathol Inc 26:1355–1364. https://doi.org/10.1038/modpathol.2013.72

34. Lam JS, Klatte T, Patard J-J, et al (2007) Prognostic Relevance of Tumour Size in T3a Renal Cell Carcinoma: A Multicentre Experience. Eur Urol 52:155–162. https://doi.org/10.1016/j.eururo.2007.01.106

35. Berenguer R, Pastor-Juan M del R, Canales-Vázquez J, et al (2018) Radiomics of CT Features May Be Nonreproducible and Redundant: Influence of CT Acquisition Parameters. Radiology 288:407–415. https://doi.org/10.1148/radiol.2018172361

36. Shafiq-ul-Hassan M, Zhang GG, Latifi K, et al (2017) Intrinsic dependencies of CT radiomic features on voxel size and number of gray levels. Med Phys 44:1050–1062. https://doi.org/10.1002/mp.12123